SANDIA REPORT

SAND2013-5375
Unlimited Release
Printed July 2013

Toward a Predictive Understanding of Low Emission Fuel-Flexible Distributed Energy Turbine Systems

Anthony Defilippo, Guilhem Lacaze, and Joseph C. Oefelein

Prepared by
Sandia National Laboratories
Albuquerque, New Mexico 87185 and Livermore, California 94550

Sandia National Laboratories is a multi-program laboratory managed and operated by Sandia Corporation, a wholly owned subsidiary of Lockheed Martin Corporation, for the U.S. Department of Energy's National Nuclear Security Administration under contract DE-AC04-94AL85000.

Approved for public release; further dissemination unlimited.

Sandia National Laboratories

Issued by Sandia National Laboratories, operated for the United States Department of Energy by Sandia Corporation.

NOTICE: This report was prepared as an account of work sponsored by an agency of the United States Government. Neither the United States Government, nor any agency thereof, nor any of their employees, nor any of their contractors, subcontractors, or their employees, make any warranty, express or implied, or assume any legal liability or responsibility for the accuracy, completeness, or usefulness of any information, apparatus, product, or process disclosed, or represent that its use would not infringe privately owned rights. Reference herein to any specific commercial product, process, or service by trade name, trademark, manufacturer, or otherwise, does not necessarily constitute or imply its endorsement, recommendation, or favoring by the United States Government, any agency thereof, or any of their contractors or subcontractors. The views and opinions expressed herein do not necessarily state or reflect those of the United States Government, any agency thereof, or any of their contractors.

Printed in the United States of America. This report has been reproduced directly from the best available copy.

Available to DOE and DOE contractors from
U.S. Department of Energy
Office of Scientific and Technical Information
P.O. Box 62
Oak Ridge, TN 37831

Telephone: (865) 576-8401
Facsimile: (865) 576-5728
E-Mail: reports@adonis.osti.gov
Online ordering: http://www.osti.gov/bridge

Available to the public from
U.S. Department of Commerce
National Technical Information Service
5285 Port Royal Rd
Springfield, VA 22161

Telephone: (800) 553-6847
Facsimile: (703) 605-6900
E-Mail: orders@ntis.fedworld.gov
Online ordering: http://www.ntis.gov/help/ordermethods.asp?loc=7-4-0#online

SAND2013-5375
Unlimited Release
Printed July 2013

Toward a Predictive Understanding of Low Emission Fuel-Flexible Distributed Energy Turbine Systems

Anthony Defilippo
Graduate Student, UC Berkeley
acflip@berkeley.edu,

Guilhem Lacaze
Combustion Research Facility
Sandia National Laboratories
MS 9051
Livermore, CA 94551-0969
gnlacaz@sandia.gov,

Joseph C. Oefelein
Combustion Research Facility
Sandia National Laboratories
MS 9051
Livermore, CA 94551-0969
oefelei@sandia.gov

Abstract

Using hydrogen derived from coal in power generation is one of the potential strategies being considered for eliminating CO2 emissions from combustion. In a two-stage gas combustor, injection of hydrogen into a secondary combustor provides an effective means for achieving a wide range of power settings. However, when additional hydrogen is injected into the exit stream of the first stage turbine, the mixture may autoignite. This uncontrolled autoignition event is undesirable as it leads to strong acoustic waves and high levels of nitrogen oxides (NOx). Since hydrogen was not a main fuel in the past, studies of hydrogen combustion under gas turbine environments have not been extensively carried out. Autoignition of hydrogen depends on pressure in a nonlinear fashion and is sensitive to the unique transport properties of the small hydrogen molecules, making prediction of autoignition a very challenging task. For both steady and transient flames, Large Eddy Simulation (LES) is essential for obtaining a fundamental understanding of flame stability mechanisms. As such, this work performs a LES study aimed at modeling and understanding 1) key stability mechanism(s) related to flame propagation and/or autoignition, and 2) the effect of pressure on hydrogen combustion over the range of 1 to 20 bar.

Contents

1 Introduction **9**

2 Theoretical and numerical approach **13**

Theoretical approach 13

Governing equations 13

Equation of state and thermodynamic properties 14

Transport Properties 14

Numerical approach 15

Preconditioning 15

Dual-time stepping 17

Spatial integration 19

Convective flux correction 20

Modified van-Leer switch (MVL) 21

Modified van-Albada switch (MVA) 21

3 Configuration description **23**

4 Results **25**

Grid sensitivity analysis 25

Flame structure at high-Re 28

Effect of strain 29

Effect of pressure 31

Combustion model definition 33

Combustion model performance 34

5 Conclusions **39**

References **41**

List of Figures

1.1 Conceptual drawing of Berkeley's Vitiated Coflow Burner (VCB). 10

1.2 Stability regimes maps for VCB for H2/N2 operation with a jet velocity of 500 m/s. 11

2.1 Data storage in the present staggered formulation in a simplified two-dimensional case. ϕ is the vector of transported scalars, V_x and V_y are the velocities in the x- and y-curvilinear directions, respectively. 19

3.1 The computational domain and dimensions: $D_j = 2.4\ mm$, coflow diameter: $d_{coflow} = 152.4\ mm$, height: $h = 800\ mm$. 23

4.1 Time-averaged plot of turbulent statistics at x/h = 5 and for varying mesh resolutions: D10 (blue line), D20 (green line), D40 (black line), D80 (red line). a) and b): mean and RMS axial velocity, c) and d) mean and RMS transverse velocity. . . 26

4.2 Instantaneous mixture fraction field in the D40 configuration (non-reacting case) white: Z=1 black: Z=0. 27

4.3 Configuration use for the analysis of the flame structure. a) Computational domain (H is the distance between inlets) and b) temperature field of a converged solution and stream-lines. 28

4.4 Strain rate effect on the H_2/O_2 counter flow flame. a) Temperature distribution in mixture fraction (Z_H) space, b) temperature distribution in physical space and c) maximum flame temperature. ($T_{O_2} = 120K$, $T_{H_2} = 295K$ and $P = 70bar$). 30

4.5 Pressure effect on the counter flow flame. a) Temperature distribution in physical space, b) and c) temperature distribution and mass fractions of principal species in mixture fraction space. ($a = 10^5 s^{-1}$). 32

4.6 Comparison between the model and the detailed computations : a) mass fraction profiles of major species, b) Sensitivity of the model to strain rate and c) sensitivity of the model to pressure. 35

4.7 Scatter plot of the heat-release with respect to mixture fraction in the DNS computations. ($\circ$) detailed chemistry, ($\bullet$) flamelet model and ($-\circ-$) counter-flow calculation $a = 1 \times 10^5\, s^{-1}$. 36

List of Tables

3.1 Inflow conditions 24

Chapter 1

Introduction

Using hydrogen derived from coal in power generation is one of the potential strategies being considered for eliminating CO2 emissions from combustion. In a two-stage gas combustor, injection of hydrogen into a secondary combustor provides an effective means for achieving a wide range of power settings. However, when additional hydrogen is injected into the exit stream of the first stage turbine, the mixture may autoignite. This uncontrolled autoignition event is undesirable as it leads to strong acoustic waves and high levels of nitrogen oxides (NOx). Since hydrogen was not a main fuel in the past, studies of hydrogen combustion under gas turbine environments have not been extensively carried out. Autoignition of hydrogen depends on pressure in a nonlinear fashion and is sensitive to the unique transport properties of the small hydrogen molecules, making prediction of autoignition a very challenging task. For both steady and transient flames, Large Eddy Simulation (LES) is essential for obtaining a fundamental understanding of flame stability mechanisms. As such, we have performed a LES study, in collaboration with UC-Berkeley, to model and understand 1) key stability mechanism(s) related to flame propagation and/or autoignition, and 2) the effect of pressure on hydrogen combustion over the range of 1 to 20 bar.

For power-generating turbine systems, the complexity of turbulence-chemistry interactions in lifted turbulent jet flames is a key challenging issue in adopting hydrogen as a potential alternative fuel. The small size of hydrogen molecules as compared to traditional carbon-containing gaseous fuels presents engineering challenges. Hydrogen molecules have higher diffusivity than other molecules, so hydrogen combustion simulations must properly account for the different transport properties. LES, coupled with innovative capabilities in treating differential diffusion with a proper subgrid-scale model, are critical in understanding the stability mechanism in lifted hydrogen jet flames. Development of accurate subgrid-scale models for hydrogen diffusion will allow for accurate and efficient engineering calculations towards designing future low-carbon power systems.

This project is aimed at the development of high fidelity models for detailed treatment of turbulent combustion in distributed energy turbine systems. Our approach involves close coupling between simulations and experiments, with strong complementary collaborations between UC Berkeley and Sandia. We apply the Large Eddy Simulation (LES) technique using the RAPTOR code framework developed by Oefelein [1] and focus on core modeling issues related to lifted flame stability in the Berkeley Vitiated Coflow Burner (VCB). The VCB is a laboratory burner designed for simulating lifted flames and was developed by Cabra et al. [2, 3] using a simple vitiated coflow, as shown in Figure 1.1. The VCB is designed with a central jet to study the effects of coflow tem-

perature, coflow velocity, and jet velocity on the liftoff height under ambient pressure conditions. Past work was done with collaborations among UC Berkeley, Sandia, and SINTEF (which is the largest independent research organization in Scandinavia). Past experimental studies were limited to stable lifted jet flames, and numerical simulations were conducted using the Reynolds-Averaged Navier-Stokes (RANS) approximation using a joint scalar probability density function approach to model turbulence-chemistry interactions. For highly unsteady turbulent flames, the limitations of RANS are significant and well appreciated in the modeling community. The use of RANS is unlikely to provide the needed transient information for understanding the complex interactions between turbulence and chemistry (i.e., turbulence-chemistry interactions) in a highly transient lifted turbulent jet flame. The challenging nature of hydrogen combustion stated in the Problem Statement (Section 1.1) provides a unique opportunity for development and use of LES to predict the stability mechanisms of such flames.

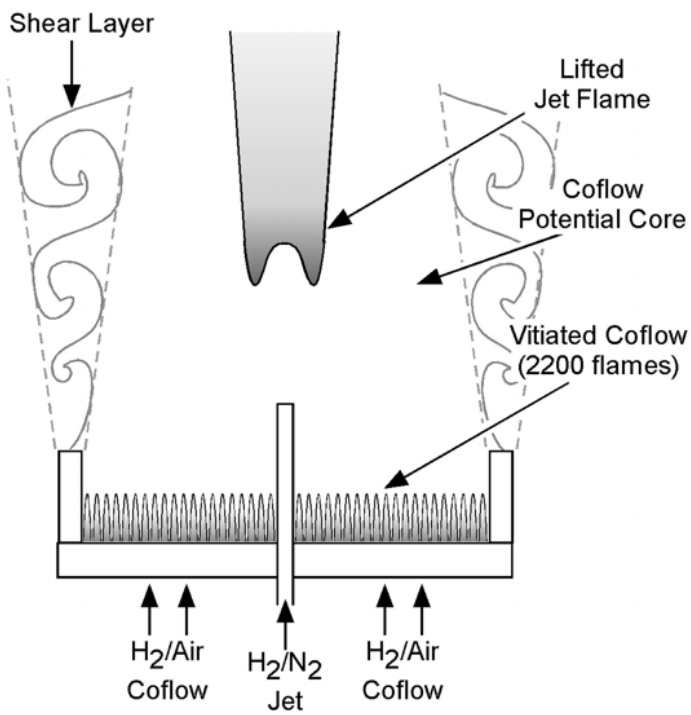

Figure 1.1. Conceptual drawing of Berkeley's Vitiated Coflow Burner (VCB).

Using the VCB experiment as the primary target, LES was performed with emphasis placed on systematic model development and joint analysis of measured and modeled results. Calculations were performed using a single unified code framework called RAPTOR. The theoretical formulation and baseline subgrid-scale (SGS) models are described by Oefelein [1]. The theoretical framework solves the fully coupled conservation equations of mass, momentum, total-energy and species for a chemically reacting flow using multicomponent or mixture-averaged formulations. It is designed to handle high-Reynolds number, high-pressure, real-gas and/or liquid conditions over

a wide Mach operating range. It also accounts for detailed thermodynamics and transport processes at the molecular level and is sophisticated in its ability to handle a generalized SGS model framework. A noteworthy aspect of RAPTOR is it was designed specifically for LES using a non-dissipative, discretely conservative, staggered, finite-volume differencing stencil. This eliminates numerical contamination of the SGS models due to artificial dissipation and provides discrete conservation of mass, momentum, energy and species, which is an imperative requirement for LES. The code has been optimized to provide excellent parallel scalability performance on a variety of computer platforms. Representative case studies are given by Oefelein et al. [4-6].

The VCB has been used to study stability limits at ambient pressure for practical burners. Recently, Schlieren imaging has been used as an effective diagnostic for studying attached, lifted, and unsteady hydrogen jet flames with a vitiated coflow at ambient pressure [7]. Using this diagnostic with a high-speed camera, the stability map shown in Figure 1.2 was generated that shows the combustion modes at various coflow equivalence ratios and dilution mole fractions. Liftoff heights have also been measured for coflow streams with equivalence ratios between 0 and 0.25. It is postulated that flame propagation stabilizes the flame for coflow equivalence ratios below 0.2, and (for this particular geometry) that autoignition dominates for higher equivalence ratios. Strong acoustic interactions were observed when the turbulent flame falls in the unsteady regime, presenting a challenging opportunity for numerical study of the possible mechanism(s).

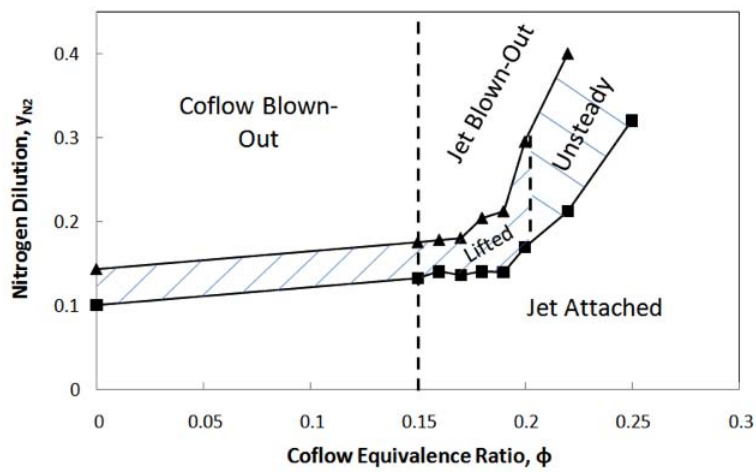

Figure 1.2. Stability regimes maps for VCB for H2/N2 operation with a jet velocity of 500 m/s.

The above survey of stability limits by Schlieren imaging also reveals a strong unsteady regime between the jet attached mode and jet blow out when the coflow equivalence ratio is beyond 0.2. To investigate this further, a high-pressure burner rated up to 8 bar has been designed by North [8] and Frederick [9] and is currently being constructed at SINTEF. A companion transient burner rated at 2 bar is being constructed at Berkeley to provide transient flame data complimentary to the steady results. For both steady and transient flames, we propose to use LES to assist in understanding the flame stability and the associated acoustics. During the development, we will address

technically challenging issues related to the modeling of hydrogen turbulent flames, namely the effect of differential diffusion and the suitable sub-grid turbulence-chemistry interaction models. The accompanying experimental data will be essential for validating the LES model. We anticipate that the results of the proposed LES simulations will identify the controlling physics in 1) key stability mechanism(s) related to flame propagation and/or autoignition, and 2) the effect of pressure on hydrogen-fuelled turbulent combustion processes.

The present report is organized as followed: in Section 2, the theoretical and numerical frameworks are presented. Then, the computational domain and boundary conditions are outlined in Section 3. Finally, in Section 4 the main results are presented. A systematic approach is employed to determine the optimal grid spacing that will provide the maximum accuracy for the minimum computational cost. The grid spacing is determined from a grid convergence study based on the first moments of turbulence. Then, a combustion model is derived based on a detailed analysis of the flame structure under realistic conditions of strain and pressure. The performance of the model is compared to detailed chemistry results and its sensitivity to strain and pressure is evaluated.

Chapter 2

Theoretical and numerical approach

Theoretical approach

The theoretical framework of the present study has been developed by Oefelein [16, 17]. This framework provides unified treatment of high Reynolds-number, high-pressure, real-gas/liquid, reacting flows over a wide Mach operating range.

Governing equations

Newtonian flows can be described by the evolution of the conserved variables: density (ρ), momentum ($\rho\mathbf{V}$), species (ρY_i, where i is the index of ith species of the mixture) and total energy (ρE, $E = e + \mathbf{V}\cdot\mathbf{V}/2$ where e is the internal energy). The governing system employed in the present study is:

$$\frac{\partial \rho}{\partial t} + \nabla\cdot(\rho\mathbf{V}) = 0, \tag{2.1}$$

$$\frac{\partial}{\partial t}(\rho\mathbf{V}) + \nabla\cdot[\rho\mathbf{u}\otimes\mathbf{V} + P\mathbf{I}] = \nabla\cdot\tau, \tag{2.2}$$

$$\frac{\partial}{\partial t}(\rho Y_i) + \nabla\cdot(\rho Y_i\mathbf{V}) = \nabla\cdot\mathbf{q}_i + \dot{\omega}_i. \tag{2.3}$$

$$\frac{\partial}{\partial t}(\rho E) + \nabla\cdot[(\rho E + P)\mathbf{V}] = \nabla\cdot[\mathbf{q}_E + \tau\cdot\mathbf{V}] + \dot{\omega}_T, \tag{2.4}$$

In this system,

$$\tau = \mu\left[-\frac{2}{3}(\nabla\cdot\mathbf{V})\mathbf{I} + \left(\nabla\mathbf{V} + \nabla\mathbf{V}^T\right)\right] \tag{2.5}$$

represents the viscous stress tensor where μ is the dynamic viscosity. P is the pressure. $\mathbf{q}_i$ and $\dot{\omega}_i$ represents the mass diffusion fluxes and chemical rate of production of the ith species, respectively.

$\mathbf{q}_i$ contains the velocity correction V_{corr} (to ensure global mass conservation) resulting from the Hirschfelder and Curtiss approximation [18]:

$$\mathbf{q}_i = -\rho \left(D_i \frac{W_i}{W} \nabla X_i - Y_i V_{corr} \right), \tag{2.6}$$

where X_i, D_i and W_i are the molar fraction, the molar diffusivity and the molar mass of the ith species, respectively and W is the molar mass of the mixture. The term $\mathbf{q}_E$ is the energy diffusion flux expressed as:

$$\mathbf{q}_E = -\lambda \nabla T + \sum_{i=1}^{N} \mathbf{q}_i h_i, \tag{2.7}$$

where λ is the thermal conductivity of the mixture, T the temperature and h_i the enthalpy of the ith species. $\dot{\omega}_T = -\sum_{i=1}^{N} \Delta h^o_{f,i} \dot{\omega}_i$, is the heat release, where $\Delta h^o_{f,i}$ is the enthalpy of formation.

Equation of state and thermodynamic properties

The equation of state employed in the present study is the Peng-Robinson (*PR*) cubic equation [19]:

$$P = \frac{RT}{V-b} - \frac{a}{V^2 + 2bV - b^2}, \tag{2.8}$$

where R is the ideal-gas constant, V the molar volume and T and P the temperature and the pressure, respectively. The coefficients a and b are coefficients that account for attraction and repulsion effects among molecules. They are calculated using a set of nonlinear mixing-rules that can be found in Reid *et al.* [19, Chapter 4]. This equation has been chosen because it is more more suitable for conditions when the temperature is greater than the critical temperature, which is the case in the flame. A summary of the cubic equations of state and recommended constants is also given by Reid *et al.* [19, Chapter 3].

A two step approach is used to determine the thermodynamic properties at relevant conditions. First, the mixture properties are evaluated at the temperature of interest and at a reference pressure, using the corresponding states methodology. A departure function is is then applied to obtain the mixture state at the desired pressure [19]. These functions are exact relations derived using the Maxwell relations and make full use of the real mixture *p-v-T* path dependencies dictated by the equation of state.

Transport Properties

Molecular transport properties are evaluated in a manner analogous to the thermodynamic properties. Viscosity and thermal conductivity are obtained using the extended corresponding states methodologies developed by Ely and Hanley [5]. Mass and thermal diffusion coefficients are obtained using methodologies from the work of Hirschfelder et al. [9] and Takahashi [25]. This approach can handle general systems where multicomponent and/or preferential diffusion processes are present.

Numerical approach

The present numerical framework has been optimized to meet the algorithm requirements imposed by the LES formalism necessary to simulate high-Reynolds number, high-pressure real-gas flows present in advanced propulsion and power devices. To facilitate the description of the numerical methods employed in the present work, the system of equation presented in section 2 is recast in integral Cartesian form for an arbitrary volume $\mathcal{V}$:

$$\frac{\partial}{\partial t}\int_{\mathcal{V}} \mathbf{Q}\, d\mathcal{V} + \int_{\partial\mathcal{V}} (\mathbf{F}_C - \mathbf{F}_D)\cdot d\mathbf{S} = 0 \tag{2.9}$$

where

$$\mathbf{Q} = \begin{bmatrix} \rho \\ \rho u \\ \rho v \\ \rho w \\ \rho E \\ \rho Y_i \end{bmatrix}, \quad \mathbf{F}_C = \begin{bmatrix} \rho\mathbf{V} \\ \rho V_x\mathbf{V} + P\,\hat{\mathbf{i}} \\ \rho V_y\mathbf{V} + P\,\hat{\mathbf{j}} \\ \rho V_z\mathbf{V} + P\,\hat{\mathbf{k}} \\ \rho E\mathbf{V} + P\mathbf{V} \\ \rho Y_i\mathbf{V} \end{bmatrix}, \quad \mathbf{F}_D = \begin{bmatrix} 0 \\ \tau_{xi} \\ \tau_{yi} \\ \tau_{zi} \\ \tau_{ij}V_j + \mathbf{q}_E \\ \mathbf{q}_i \end{bmatrix}$$

with

$$\mathbf{V} = (V_x, V_y, V_z)^T, \tag{2.10}$$

and the viscous stress tensor τ, the species diffusion flux $\mathbf{q}_i$ and the heat flux vector $\mathbf{q}_E$ have been previously defined in Eq. 2.5, 2.6 and 2.7, respectively.

Preconditioning

The above system defined by Eq. 2.9 is well conditioned for high-speed flows where the information of pressure and fluid particles travel at speeds of the same order. In the case of low Mach number flows, stiffness arises in the system due to the disparity between acoustic and gas velocities. In other word the eigenvalues of the system ($u+c$, $u-c$, u,u,u,u, etc.) become very different at low speed and as a result the time-marching algorithm convergence performance is severely impaired. A similar problem occurs in region of the flow where viscous diffusion time scale become much smaller than convective time scale. This situation can be encountered in boundary layers near walls and other flow regions where velocities are small with strong field gradients.

One method to improve the convergence rate of the time integration step is to apply a preconditioning matrix to the system (2.9) [3]. The objective of this approach is to recast the governing system to force all eigenvalues to be of the same order. As this technique artificially modifies the time-derivative terms, the method cannot be employed to accurately resolve unsteady flows. To recover the time accuracy of the governing equations, a dual-time stepping method is employed. The main advantage of preconditioning is that the convergence rate is optimal compared to other

conventional approaches and the time-step that is not constrained by CFL limitation but only by temporal accuracy [14].

The derivation of the preconditioning matrix follows the methodology presented in [15]. Two steps are required. First the system is recast to extract a set of new variables that permit to expose the eigenvalues of the system. The proposed vector is $\mathbf{Q_v} = (P, V_x, V_y, V_z, T, Y_i)^T$. The choice of pressure is fairly natural as it allows to isolate the propagation of acoustics waves. The temperature T greatly simplifies the computation of Jacobians and transformation matrices. Enthalpy has been used by other researchers [31].

The transformation Jacobian is:

$$\mathbf{T} = \frac{\partial \mathbf{Q}}{\partial \mathbf{Q_v}}, \tag{2.11}$$

The first term of $\mathbf{T}$ is the coefficient of the pressure time-derivative in the continuity equation: G/c^2 that reflects the propagation speed of pressure waves. The second step of the preconditioning is to alter this term in order to obtain eigenvalues of the same order for all Mach number conditions even when viscous effects are dominant. Practically the speed of sound term c^2 is replaced by a parameter β that is scaled depending on local flow conditions. The altered transformation matrix is called the preconditioning matrix $\mathbf{G}$:

$$\mathbf{G} = \begin{bmatrix} \frac{G}{\beta} & 0 & 0 & 0 & -\frac{\rho}{T}\mathcal{Z}_T & -\rho\mathcal{R}_1 & \cdots & -\rho\mathcal{R}_{N-1} \\ \frac{GV_x}{\beta} & \rho & 0 & 0 & -\frac{\rho V_x}{T}\mathcal{Z}_T & -\rho V_x\mathcal{R}_1 & \cdots & -\rho V_x\mathcal{R}_{N-1} \\ \frac{GV_y}{\beta} & 0 & \rho & 0 & -\frac{\rho V_y}{T}\mathcal{Z}_T & -\rho V_y\mathcal{R}_1 & \cdots & -\rho V_y\mathcal{R}_{N-1} \\ \frac{GV_z}{\beta} & 0 & 0 & \rho & -\frac{\rho V_z}{T}\mathcal{Z}_T & -\rho V_z\mathcal{R}_1 & \cdots & -\rho V_z\mathcal{R}_{N-1} \\ \frac{Gh_t}{\beta} - \mathcal{Z}_T & \rho V_x & \rho V_y & \rho V_z & -\frac{\rho h_t}{T}\mathcal{Z}_T + \rho C_p & -\rho h_t\mathcal{R}_1 + \rho\mathcal{H}_1 & \cdots & -\rho h_t\mathcal{R}_{N-1} + \rho\mathcal{H}_1 \\ \frac{GY_1}{\beta} & 0 & 0 & 0 & -\frac{\rho Y_1}{T}\mathcal{Z}_T & -\rho Y_1\mathcal{R}_1 + \rho & \cdots & -\rho Y_1\mathcal{R}_{N-1} \\ \vdots & \vdots & \vdots & \vdots & \vdots & \vdots & \ddots & \vdots \\ \frac{GY_{N-1}}{\beta} & 0 & 0 & 0 & -\frac{\rho Y_{N-1}}{T}\mathcal{Z}_T & -\rho Y_{N-1}\mathcal{R}_1 & \cdots & -\rho Y_{N-1}\mathcal{R}_{N-1} + \rho \end{bmatrix}$$

where

$$\beta = \frac{G\varepsilon c^2}{1 + (G-1)\varepsilon}, \tag{2.12}$$

$$\mathcal{Z}_T = 1 + \frac{T}{Z}\left(\frac{\partial Z}{\partial T}\right)_P, \tag{2.13}$$

$$\mathcal{R}_i = \frac{R_i - R_N}{R}\left[1 + \frac{R}{(R_i - R_N)Z}\frac{\partial Z}{\partial Y_i}\right]_{P,T,Y_{j,j\neq i}}, \tag{2.14}$$

$$\text{with } R_i = \frac{ZR_u}{W_i} \text{ and } R = \sum_{i=1}^{N} R_i Y_i, \tag{2.15}$$

$$\mathcal{H}_i = h_i - h_N \tag{2.16}$$

The terms Z, h_i and G are the compressibility factor, the enthalpy of the species i and the ratio of specific heats, respectively. The complete derivation of matrix $\mathbf{G}$ can be found in [15]. As discussed before, by replacing the speed of sound c^2 by β, one can control the conditioning of the eigenvalues of the system. In the definition of β, the parameter ε, where $0 < \varepsilon < 1$, allows one to optimally scales eigenvalues depending on flow conditions (Reynolds and Mach numbers). The definition of ε has been derived using the work of Choi and Merkle [4], Buelow et al. [1] and Venkateswaran and Merkle [29]. The eigenvalues of this new system are given in [15].

Contrary to conventional approaches, the present method retains all the term of the transformation matrix so that the physical system is recovered when $\varepsilon \to 1$, which translates to:

$$lim_{\varepsilon \to 1} \mathbf{G} = \mathbf{T}, \tag{2.17}$$

Dual-time stepping

Using previous preconditioning technique the system can efficiently be driven to steady state using the following framework:

$$\mathbf{G} \frac{\partial}{\partial \tau} \int_{\mathcal{V}} \mathbf{Q_v} \, d\mathcal{V} + \int_{\partial \mathcal{V}} (\mathbf{F}_C - \mathbf{F}_D) \cdot d\mathbf{S} = 0 \tag{2.18}$$

Here τ is the numerical time step also called pseudo-time, and does not represent the physical time. However, as the preconditioning method has modified the Navier-Stokes equations, the physical time-derivative terms must be re-introduced in the system to recover the temporal accuracy for unsteady simulations [29]:

$$\mathbf{G} \frac{\partial}{\partial \tau} \int_{\mathcal{V}} \mathbf{Q_v} \, d\mathcal{V} + \frac{\partial}{\partial t} \int_{\mathcal{V}} \mathbf{Q} \, d\mathcal{V} + \int_{\partial \mathcal{V}} (\mathbf{F}_C - \mathbf{F}_D) \cdot d\mathbf{S} = 0 \tag{2.19}$$

By approximating this system in delta-form at the $n+1$ real-time level, the problem to solve in semi-descrite form becomes:

$$\mathbf{G} \left(\frac{\partial \mathbf{Q_v}}{\partial \tau} \right)^{n+1} + \mathbf{R}_*^{n+1} = 0 \, , \tag{2.20}$$

$$\text{with} \quad \mathbf{R}_*^{n+1} = \left(\frac{\partial \mathbf{Q}}{\partial t} \right)^{n+1} + \frac{1}{\Delta_{\mathcal{V}}} \mathbf{R}^{n+1} \, , \tag{2.21}$$

where $\mathbf{R}^{n+1}$ is the residual term combining convective, viscous and stabilization fluxes at the physical step $n+1$. Using this system, each time step in physical time can be seen as a steady state solution in pseudo-time that can be efficiently converged using the properties of the preconditioning matrix. Note that at steady state in pseudo-time the term $\frac{\partial \mathbf{Q_v}}{\partial \tau} \to 0$ and the unsteady governing equation system is recovered.

The objective of the dual-time stepping method is to efficiently resolve the system (2.20) [30]. This approach involves an inner iteration loop in pseudo time that is wrapped around an outer loop in physical time. Each physical time step is treated as a steady-state problem in pseudo-time. N inner-loop iterations are required to converge the system to the next physical step. In Eq. 2.19 the pseudo-time marching is evaluated using an explicit four-stage Runge-Kutta scheme [10, 6]:

$$
\begin{aligned}
\mathbf{q}^{(0)} &= (\mathbf{Q_v^{n+1}})^m \\
\mathbf{q}^{(1)} &= \mathbf{q}^{(0)} + \frac{1}{2}\Delta\tau\mathbf{R}_*(\mathbf{q}^{(0)}) \\
\mathbf{q}^{(2)} &= \mathbf{q}^{(0)} + \frac{1}{2}\Delta\tau\mathbf{R}_*(\mathbf{q}^{(1)}) \\
\mathbf{q}^{(3)} &= \mathbf{q}^{(0)} + \Delta\tau\mathbf{R}_*(\mathbf{q}^{(2)}) \\
\mathbf{q}^{(4)} &= \mathbf{q}^{(0)} + \frac{1}{6}\mathbf{q}^{(1)} + \frac{1}{3}\mathbf{q}^{(2)} + \frac{1}{3}\mathbf{q}^{(3)} + \frac{1}{6}\Delta\tau\mathbf{R}_*(\mathbf{q}^{(3)}) \\
(\mathbf{Q_v^{n+1}})^{m+1} &= \mathbf{q}^{(4)}
\end{aligned}
$$

where the superscript m denotes the pseudo-time level $m\Delta\tau$ and $\mathbf{R}_*$ is defined by Eq. 2.21. The physical time derivatives are estimated using a three-point backward implicit difference with second-order accuracy [30]:

$$
\left(\frac{\partial \mathbf{Q}}{\partial t}\right)^{n+1} = \frac{1}{\Delta_t}\left(\frac{3}{2}\mathbf{Q}^{n+1} - 2\mathbf{Q}^n + \frac{1}{2}\mathbf{Q}^{n-1}\right) \tag{2.22}
$$

Using this approach, the temporal marching in physical time is not affected by the stiffness caused by the disparity in eigenvalues since the convergence of the inner-loop has been optimized by preconditioning. When the system is hyperbolic ($Re \gg 1$, viscous effects are negligible), the stability depends on the Courant-Friedrichs-Lewy (CFL) number: $CFL = \frac{\lambda\Delta\tau}{\Delta_x}$, with λ being the spectral radius of acoustics waves in the preconditioned system (also called the pseudo-acoustic speed) and Δ_x being the local grid spacing. In the present framework, the pseudo-acoustic speed is:

$$
\lambda = \frac{\rho}{2}\left[|U_\eta|(1+\varepsilon) + \sqrt{U_\eta^2(1-\varepsilon)^2 + 4\varepsilon c^2 r_x^2}\right] , \tag{2.23}
$$

where U_η is the convective velocity in the acoustic propagation direction and r_x the local grid aspect ratio. The derivation of the pseudo-acoustic time can be found in [15]. Buelow et al. [1] have shown that for the present system, the optimal value is in the range: $1 \leq CFL_{max} \leq 10$.

When the system becomes parabolic (at low Re, viscous effects are non-negligible), stability depends on the von-Neumann number: $VNN = \frac{\nu\Delta\tau}{\Delta_x^2}$. Jameson *et al.*[10] have shown that the stability range in the case of preponderant viscous effects is: $VNN_{max} \leq 0.25$. Finally, the optimal local pseudo-time step can be estimated by applying the constraints:

$$
\Delta\tau = min\left(\frac{CFL_{max}\Delta_x}{\lambda}; \frac{VNN_{max}\Delta_x^2}{\nu}\right) \tag{2.24}
$$

The von-Neumann stability analysis of the complete system has been carried out by Oefelein [15].

Spatial integration

The present governing system is discretized on a structured staggered grid in general curvilinear coordinates using a finite-volume approach. Scalar information is stored at cell-centroids while velocities are stored at cell-face centers as shown in Fig. 2.1. Using this framework, the system

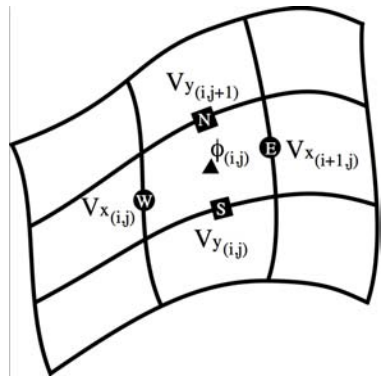

Figure 2.1. Data storage in the present staggered formulation in a simplified two-dimensional case. ϕ is the vector of transported scalars, V_x and V_y are the velocities in the x- and y-curvilinear directions, respectively.

described in Eq. 2.19 can be discretized in space as:

$$\mathbf{G}\frac{\partial \tilde{\mathbf{Q}}_{\mathbf{v}}}{\partial \tau} + \frac{\partial \tilde{\mathbf{Q}}}{\partial t} + \frac{1}{\mathcal{V}} \sum_{faces} (\overline{\mathbf{F}}_C - \overline{\mathbf{F}}_D) \cdot \mathbf{A} = 0 \,, \tag{2.25}$$

where the vectors $\tilde{\mathbf{Q}}_{\mathbf{v}}$ and $\tilde{\mathbf{Q}}$ are averaged over the cell volume $\mathcal{V}$. Note that due to staggering, cell volumes for scalars and velocities may be different in case of a stretched grid. $\overline{\mathbf{F}}_C$ and $\overline{\mathbf{F}}_D$ are the discrete flux vectors that are assumed to be constant over each face with $\mathbf{A}$ the local face area vector. This approach provides non-dissipative and discrete conservation of mass, momentum and total energy [7]. This framework however does not ensure a stable solution in the presence of large gradients in the transported quantities. At supercritical conditions, very steep gradients of density are present in the field which must be treated appropriately to guarantee accuracy and stability of the computation.

In the present work, stabilization is ensured by special treatment of convective fluxes based on a flux difference splitting method [21, 22]. For example, the value of the inviscid flux $\overline{\mathbf{F}}_C^W$ through the face W (see Fig. 2.1) is given by:

$$\overline{\mathbf{F}}_C^W = \frac{1}{2}\left[\mathbf{F}_C(\tilde{\mathbf{Q}}_{\mathbf{v}}^L) + \mathbf{F}_C(\tilde{\mathbf{Q}}_{\mathbf{v}}^R)\right] \,, \tag{2.26}$$

where the superscripts L and R represent the left and right states of face W, respectively.

Two approaches can be considered to define the stabilization term: scalar dissipation models [10] and matrix dissipation models [24]. In the present work the matrix dissipation method has been employed since it allows different magnitudes of dissipation for each discrete equation, and theoretically permits one to minimize the amount of dissipation compared to the scalar approach. Depending on the manner in which the terms of Eq. 2.26 are evaluated, a wide variety of central difference and upwind schemes can be derived. The detail of the flux splitting method is presented in the following section.

Convective flux correction

The present dissipation method is based on the composition of a high-order scheme and a robust upwind scheme [24]. In simplified notations, the inviscid flux on a given cell face can be expressed as:
$\mathbf{F}_C = \mathbf{F}_C^{high} + \nu(\mathbf{F}_C^{low} - \mathbf{F}_C^{high})$, where $\mathbf{F}_C^{high}$ and $\mathbf{F}_C^{low}$ are the contributions of the high-order and low-order schemes, respectively. ν is a sensor defined on the interval $0 \leq \nu \leq 1$. This term switches the truncation error from high-order accuracy when $\nu \to 0$, in smooth regions of the flow, to low-order accuracy when $\nu \to 1$ in shocks and steep gradients. In the present study, $\mathbf{F}_C^{high}$ is the third-order accurate *QUICK* scheme and $\mathbf{F}_C^{low}$ a first-order upwind scheme. Historically, upwind algorithms have been developed in the context of shock capturing, and utilize concepts from characteristic theory [21, 28].

Practically, in the present solver, the convective flux for any conserved scalar $\tilde{\phi}$ is evaluated using the following upwind approach:

$$\overline{\mathbf{F}}_{C,\phi}^{W} = V_x^W \, \tilde{\phi}^L \text{ , if } V_x^W > 0 \, , \tag{2.27}$$

$$\overline{\mathbf{F}}_{C,\phi}^{W} = V_x^W \, \tilde{\phi}^R \text{ , if } V_x^W < 0 \, . \tag{2.28}$$

The formulation for momentum terms is similar and thus not described here. Note, however, that cross-terms for momentum fluxes require an additional interpolation step. In the following, the tilde finite-volume operand ($\tilde{}$) will be abandoned for sake of clarity.

The flux limiter is incorporated in the definition of ϕ^L and ϕ^R, defined here in an one-dimensional context:

$$\phi^L = \phi_{i-1/2}^L = \frac{1}{2}(\phi_i + \phi_{i-1}) - \frac{1-\nu_{i-1/2}(\phi)}{8}(\phi_i - 2\phi_{i-1} + \phi_{i-2}) - \frac{\nu_{i-1/2}(\phi)}{2}(\phi_i - \phi_{i-1}) \, , \tag{2.29}$$

$$\phi^R = \phi_{i-1/2}^R = \frac{1}{2}(\phi_i + \phi_{i-1}) - \frac{1-\nu_{i-1/2}(\phi)}{8}(\phi_{i+1} - 2\phi_i + \phi_{i-1}) - \frac{\nu_{i-1/2}(\phi)}{2}(\phi_i - \phi_{i-1}) \, . \tag{2.30}$$

One can observe that when $\nu_{i-1/2}(\phi) = 0$ (in smooth regions of the flow), the third-order

accurate *QUICK* formulation is recovered:

$$\phi^L = \frac{1}{2}(\phi_i + \phi_{i-1}) - \frac{1}{8}(\phi_i - 2\phi_{i-1} + \phi_{i-2}) = \frac{3}{8}\phi_i + \frac{3}{4}\phi_{i-1} - \frac{1}{8}\phi_{i-2}\,, \tag{2.31}$$

and in gradient zones, $\nu_{i-1/2}(\phi) = 1$, a stable first-order accurate upwind scheme is used:

$$\phi^L = \frac{1}{2}(\phi_i + \phi_{i-1}) - \frac{1}{2}(\phi_i - \phi_{i-1}) = \phi_{i-1} \tag{2.32}$$

In practice, switch values are estimated at cell centroids and then interpolated at cell faces:

$$\nu_{i-1/2}(\phi) = min\left(1, max\left(0, \frac{\nu_i(\phi) + \nu_{i-1}(\phi)}{2}\right)\right) \tag{2.33}$$

In the present context gradients are intensified by turbulence, the main challenge is to define an optimal switch ν that detects under-resolved region of the flow. Jorgenson and Turkel have compared the different existing switching approaches and have proposed a modified formulation of the van-Leer (MVL) and van-Albada (MVA) switches that present the best properties for hyperbolic problems [11]. These switches are used in the present study.

Modified van-Leer switch (MVL)

This switching method was first developed by van Leer [27] and then improved by Jorgenson and Turkel [11]. In a one-dimensional finite difference framework, it is defined as:

$$\nu_i^{MVL}(\phi) = \frac{|\phi_{i+1} - 2\phi_i + \phi_{i-1}|}{(1-\alpha^{MVL})(|\phi_{i+1} - \phi_i| + |\phi_i - \phi_{i-1}|) + \alpha^{MVL}(\phi_{i+1} + 2\phi_i + \phi_{i-1}) + \varepsilon}\,, \tag{2.34}$$

where ϕ is a flow variable (T, ρ and Y_i), α^{MVL} is constant parameter that allows one to tune the properties of the switch. The flux corrector is TVD when $\alpha^{MVL} = 0$, Total Variation Bounded (TVB) when $\alpha^{MVL} = 1$ and Essentially Non-Oscillating (ENO) when $0 < \alpha^{MVL} < 1$ [11]. In the present study $\alpha^{MVL} = 0.5$. $\varepsilon = 10^{-8}$ to avoid singular behavior.

Modified van-Albada switch (MVA)

This switch has been originally developed by van Albada [26], for astrophysics computations. It was later modified byJorgenson and Turkel [11]. Its expression is given by:

$$\nu_i^{MVA}(\phi) = \frac{(\phi_{i+1} - \phi_i)^2 + (\phi_i - \phi_{i-1})^2 - (\phi_{i+1} - \phi_i)(\phi_i - \phi_{i-1}) - |(\phi_{i+1} - \phi_i)(\phi_i - \phi_{i-1})|}{(\phi_{i+1} - \phi_i)^2 + (\phi_i - \phi_{i-1})^2 + \alpha^{MVA}(\phi_{i+1} + 2\phi_i + \phi_{i-1})^2 + \varepsilon}\,, \tag{2.35}$$

where α^{MVA} has a similar role to α^{MVL} is Eq. 2.34 and is set to $\alpha^{MVA} = 0.5$ in the present case. The small parameter $\varepsilon = 10^{-8}$ is also present to avoid divergence.

This page intentionally left blank.

Chapter 3

Configuration description

The computational setup is described here. First dimensions are presented in Fig. 3.1

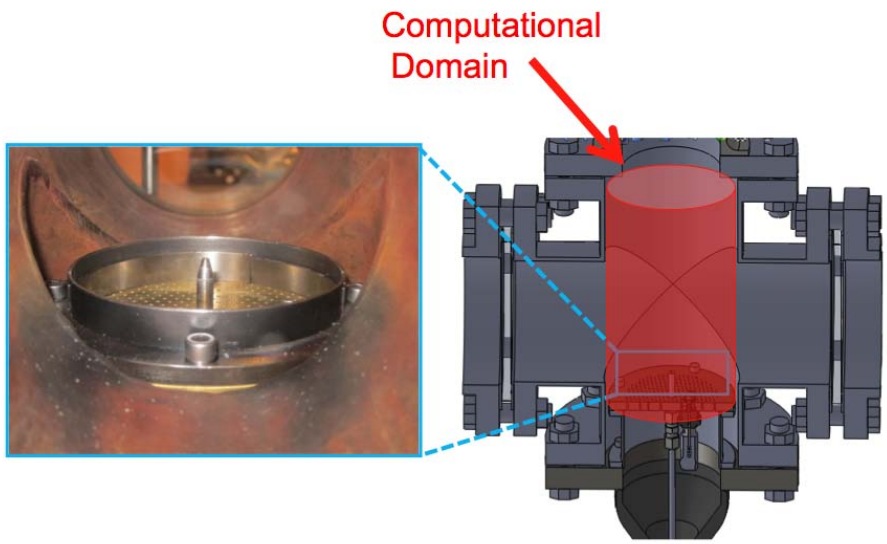

Figure 3.1. The computational domain and dimensions: $D_j = 2.4\ mm$, coflow diameter: $d_{coflow} = 152.4\ mm$, height: $h = 800\ mm$.

Synthetic turbulence is added to the inlet boundary conditions using the digital filtering technique of [12]. The boundary layer thickness in the coflow is set to 3 mm, in accordance with the experimental measurements. Only the wall that contains the jet injection is a no-slip wall, the other walls are slipping wall, so that the velocity stays constant in the vicinity of those slipping walls. In the jet, a fully developed pipe flow is assumed for the turbulent inlet profile. Note that because we inject a velocity profile instead of a plug flow, the velocity profile is scaled so that the mass flow rate is maintained to its target value. The pressure in the channel is 4.14 MPa. These conditions are summarized in Tab. 3.1.

Pressure: 41.4 bar	
Coflow, $Re \approx 18,600$	
T	1045 K
X_{O_2}	0.15
X_{N_2}	0.75
X_{H_2O}	0.1
U_x	$1/7^{th}$ profile, $U_{max} = 3.5\ m/s$
turbulence :	correlated signal, intensity= 10%
Jet, $Re \approx 23,600$	
T	305 K
X_{N_2}	0.75
X_{H_2}	0.25
U_y	$1/7^{th}$ profile, $U_{max} = 107\ m/s$
turbulence :	correlated signal, intensity= 10%

Table 3.1. Inflow conditions

Chapter 4

Results

The first step before carrying out the detailed analysis of the combustion processes is to perform a grid sensitivity study to determine the optimal grid spacing required.

Grid sensitivity analysis

In the present work, as the turbulent jet is surrounded by a coflow, classical empirical fits cannot be used to determine the characteristic size of turbulent structures required to estimate grid spacing. A different approach has been chosen to maximize result accuracy while keeping a reasonable computation cost to obtain converged time-averaged turbulent statistics. Here, the most stretched diffusive layers that fall under the grid resolution are stabilized numerically, whereas a sufficiently wide range of larger scales are resolved.

This approach is justified in a detailed flow analysis under the conditions that the stabilization method stays very localized, does not interfere with the studied physics and does not contaminate other regions of the flow. In our approach, both stabilization methods (see section 2) have been optimized to operate only on very narrow zones where gradients are under-resolved. As these methods depend directly on grid resolution, the computation converges towards DNS as the computational grid is refined. Hence, a convergence study is required to determine when the mean and RMS of velocity and scalars become insensitive to mesh spacing.

At sufficiently high resolution, scales that are not resolved are then too small to have a significant impact of mixing and can be filtered. Because the present flow is transitioning by nature, turbulent kinetic energy production is not in equilibrium with dissipation, which is the base assumption of LES turbulent closures.

A set of simulations using increasingly refined meshes have been conducted. The number of cells within the diameter of the jet D_j is set to 10, 20, 40 and 80. In the following, the meshes are called 'Dn', where n is the number of cells within the jet diameter.

The mean and RMS profiles of the major quantities of interest in the transverse direction have been compared for different mesh refinements. For sake of brevity, only the profiles of axial and transverse velocities located at $x = 5D_j$ are presented in Fig. 4.1. Very similar trends have been observed at other locations.

While there is a significant impact of mesh resolution between D10 and D20, the time-averaged results are not, at first order, sensitive to mesh resolution beyond D20. A detailed observation shows that some discrepancies exist, for instance the value of the vertical velocity for $y > 0$ is different between D20 or D40 and D80, but is quantitatively small and qualitatively identical.

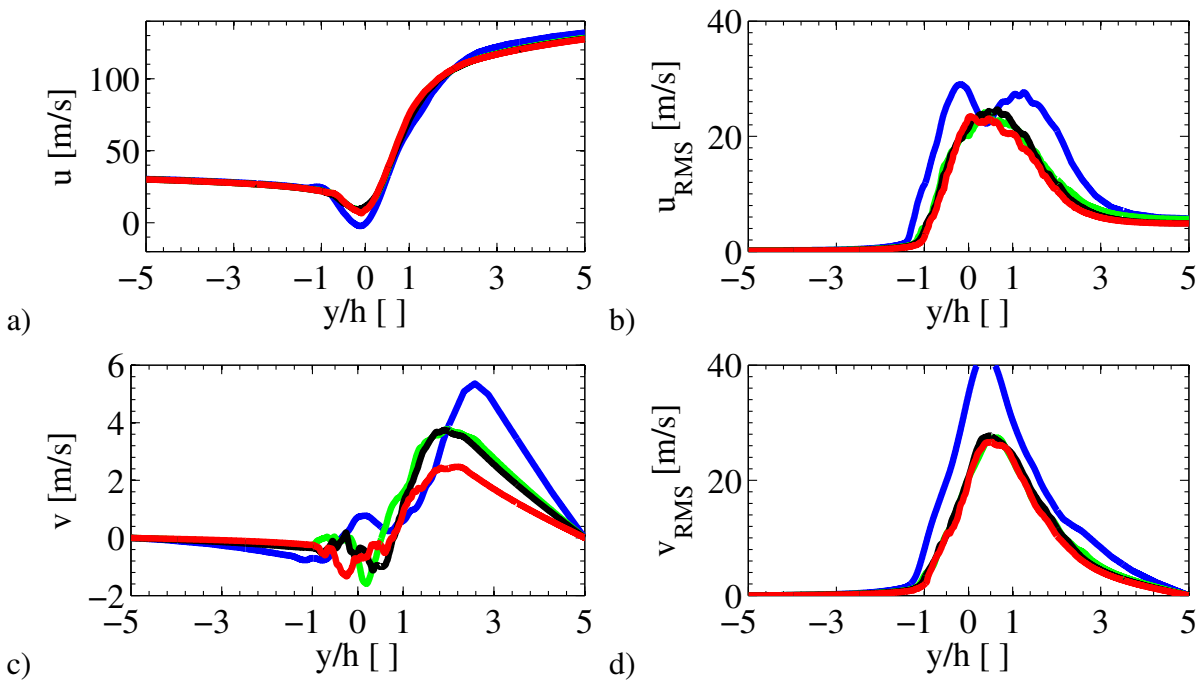

Figure 4.1. Time-averaged plot of turbulent statistics at x/h = 5 and for varying mesh resolutions: D10 (blue line), D20 (green line), D40 (black line), D80 (red line). a) and b): mean and RMS axial velocity, c) and d) mean and RMS transverse velocity.

For all the resolutions, large structures can be observed with qualitatively similar characteristics in each case. The fact that these particular entities have similar characteristics can be explained by the fact that at all resolutions, the Kelvin-Helmholtz mechanism that sheds eddies at the injector lip is captured even with the coarser mesh. The main reason is that this process only depends on geometrical parameters (channels and splitter plate height) and inlet velocity profiles, which are input parameters for the current configuration.

It is visually clear that the increase in resolution impacts turbulence at the smallest scales. Qualitatively, one can observe that between the D40 and D80 cases, grid resolution seems to impact only the smallest scales, leading to the impression that some convergence has been attained. In the following, the D40 configuration is used to perform the detail LES analysis of the flow.

An instantaneous field of mixture fraction is shown in fig. 4.2.

Figure 4.2. Instantaneous mixture fraction field in the D40 configuration (non-reacting case) white: Z=1 black: Z=0.

Flame structure at high-Re

To define a predictive combustion model for the present configuration, the detailed structure of the flame must be investigated under realistic conditions. The purpose of this section is to determine if a flamelet-type model would be relevant to represent the non-premixed portion of the flame. As Reynolds numbers does not allow a DNS study of the flame structure in the actual configuration, an opposed jet case has been designed to accurately investigate the effect of strain and pressure on the flame structure. The DNS configuration is presented in Fig. 4.3.

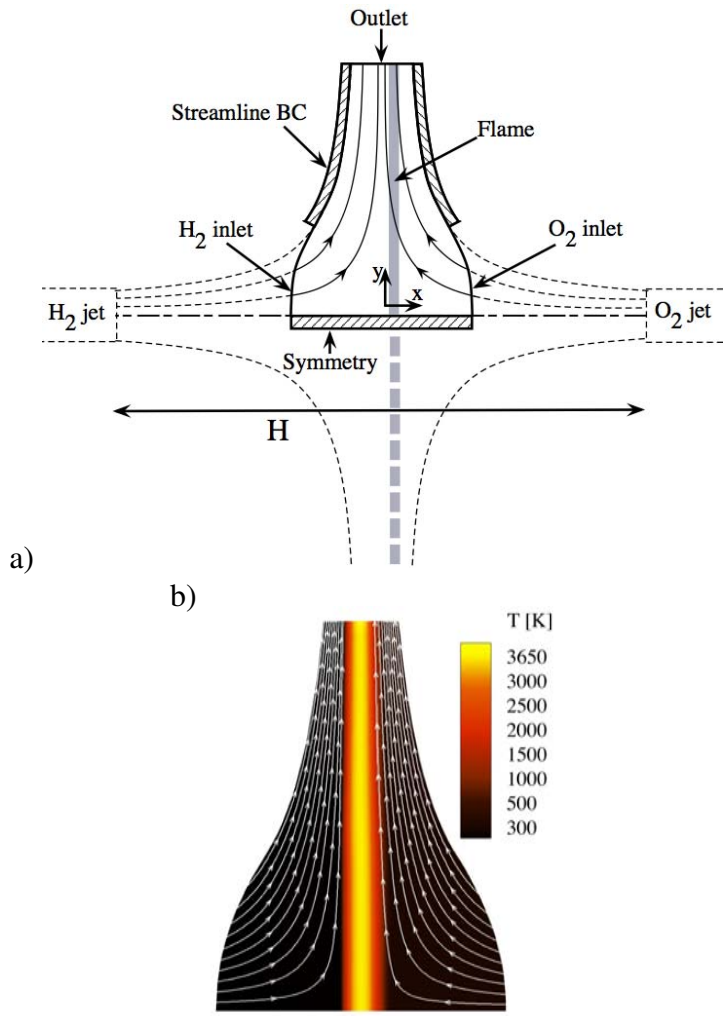

Figure 4.3. Configuration use for the analysis of the flame structure. a) Computational domain (H is the distance between inlets) and b) temperature field of a converged solution and stream-lines.

Effect of strain

The aim of this section is to study strain rate effects on the flame structure. The flame robustness to strain at the conditions of interest is studied to determine if variations in scalar dissipation rate must be taken into account in the tabulation.

Figure 4.4 shows the temperature profiles in mixture fraction space Z_H, and in physical space as well, for different strain rates at the conditions of interest ($T_{O_2} = 120K$, $T_{H_2} = 295K$ and $P = 70bar$). Note that the present flame is composed of species with very different diffusion coefficients, but the mixture fraction is based on H atoms to ensure it remains a passive scalar [18]:

$$Z_H = W_H \left(2\frac{Y_{H_2}}{W_{H_2}} + \frac{Y_H}{W_H} + 2\frac{Y_{H_2O}}{W_{H_2O}} + \frac{Y_{OH}}{W_{OH}} + \frac{Y_{HO_2}}{W_{HO_2}} + 2\frac{Y_{H_2O_2}}{W_{H_2O_2}} \right) \tag{4.1}$$

In Figure 4.4 a), one can observe that all temperature profiles collapse on the same curve for strain rates less than or equal to $10^6 s^{-1}$. Under the infinitely fast chemistry assumption, it is possible to analytically show that the heat release rate $\dot{Q}_s$ of a strained flame scales as $\sqrt{a}$ [18][1]. By definition:

$$\dot{Q}_s = \int_{-\infty}^{+\infty} \dot{\omega}_T dx \tag{4.2}$$

$$\dot{\omega}_T = \sum_{i=1}^{N_s} h_i^\circ W_i \dot{\omega}_i \tag{4.3}$$

where h_i° and $\dot{\omega}_i$ are the formation enthalpy and the the molar production rate of the ith species respectively.

Diffusion fluxes taking heat away from the flame also scale as $\sqrt{a}$ [18]. Consequently, both source and sink effects balance each other exactly, which explains why the maximum temperature remains constant. When the chemical and diffusion timescales become the same order of magnitude (as the strain rate increases), the infinitely fast chemistry assumption vanishes and heat release no longer compensates the heat losses. Thus, the maximum temperature decreases. This effect is shown in Fig. 4.4 b) where the maximum flame temperature is almost constant for $a < 10^6 s^{-1}$ and close to the equilibrium temperature, but decreases for higher strain rates ($a > 10^6 s^{-1}$).

In physical space, an increase in strain rate induces a decrease in flame thickness. An estimate of the flame thickness (δ_{flm}) can be derived from the scalar dissipation rate definition :

$$\delta_{flm} \approx \left(\frac{1}{|\nabla Z|} \right)_{Z=Z_{st}} = \sqrt{\frac{2D_{st}}{\chi_{st}}} \propto 1/\sqrt{Pa} \ , \tag{4.4}$$

where Z_{st}, D_{st} and χ_{st} are the mixture fraction, molecular diffusion coefficient, and scalar dissipation rate at the stoichiometric point. In the present work, the flame thickness follows this trend and the same observation was made by Ribert *et al.* [20].

[1] This result has been observed in the present study and in the work of Ribert *et al.* [20] and thus are not presented here for sake of conciseness.

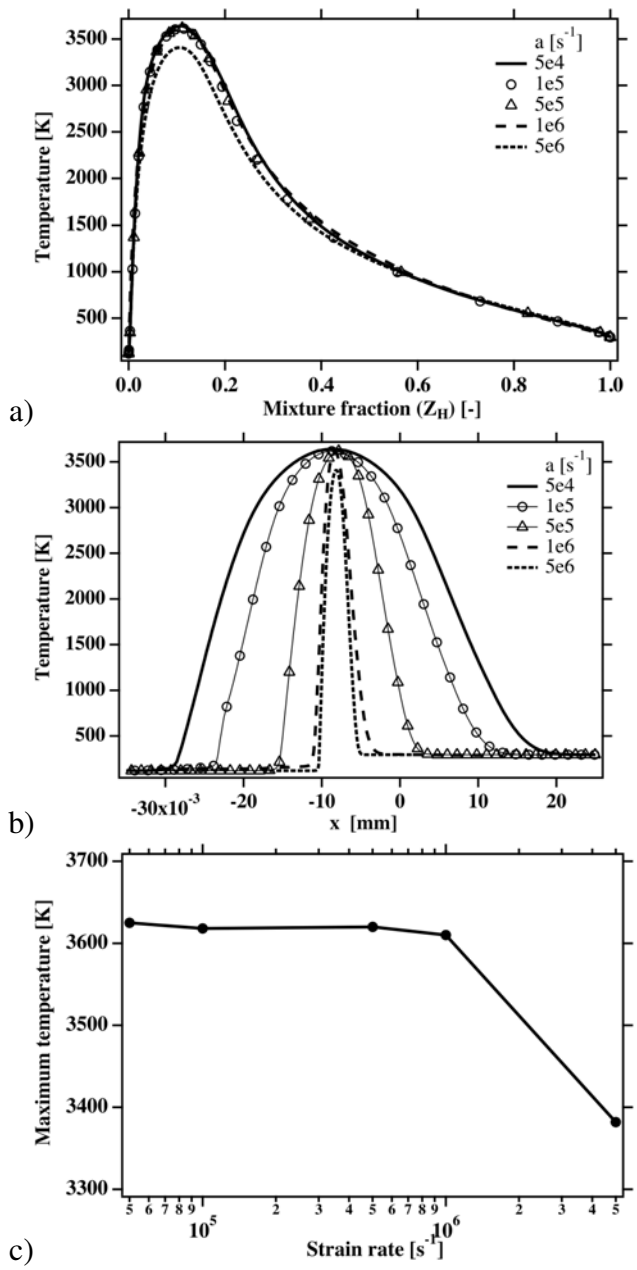

Figure 4.4. Strain rate effect on the H_2/O_2 counter flow flame. a) Temperature distribution in mixture fraction (Z_H) space, b) temperature distribution in physical space and c) maximum flame temperature. ($T_{O_2} = 120K$, $T_{H_2} = 295K$ and $P = 70bar$).

Analysis of these results verifies that the infinitely fast chemistry assumption is valid for the range of strain rates of interest ($a < 9 \times 10^5 s^{-1}$). Hence, a chemistry tabulation does not require that the strain rate be taken into account.

Effect of pressure

The present investigation aims at modeling stabilization of a vitiated hydrogen flame at elevated pressure. This subsection is dedicated to the study of the effect of pressure on flame structure.

In high-pressure systems, small pressure oscillations may perturb the flow dynamics or flame leading to combustion instabilities [8, 32]. Under certain circumstances, acoustic waves may have an effect on mixing, mass flow-rate, combustion, etc., and can result in a modulation of the heat release and subsequently a new pressure perturbation. Coupling may occur and sustained pressure oscillations may develop in the combustor. Combustion instabilities can have severe consequences on the efficiency of the burner and can lead to its destruction. Such instabilities are still not fully understood and active research is currently dedicated to this field (see for example [2, 13, 23]). Hence, pressure effects on the flame structure were investigated here in the range $53-90$ *bar*.

Figure 4.5 presents the impact of pressure on the flame structure in both physical and mixture fraction space. The first observation is that the maximum flame temperature increases with pressure (Fig. 4.5 a). However, in the range of interest, the variation of the maximum temperature is about $100\,K$ which represents a discrepancy of about 3% with respect to the flame temperature at $70\,bar$. Another effect is the modification of the flame thickness. This tendency is predicted by asymptotic analysis as shown in section 4, Eq. 4.4, and it was verified that the flame thickness is pressure dependent via the relation: $\delta_{flm} \propto 1/\sqrt{P}$. A similar derivation shows that for infinitely fast chemistry, the heat release rate follows the relation : $\dot{Q}_s \propto \sqrt{P}$ [18]. This result was observed in the present study, and is a classical trend for fast chemical systems.

In mixture fraction space, temperature profiles and mass-fraction distributions almost collapse on the same curve (fig. 4.5 b and c). This shows that only one flame is required to represent temperature and species profiles over a wide range of pressures. For the pressure range considered here, the error is less than 3%.

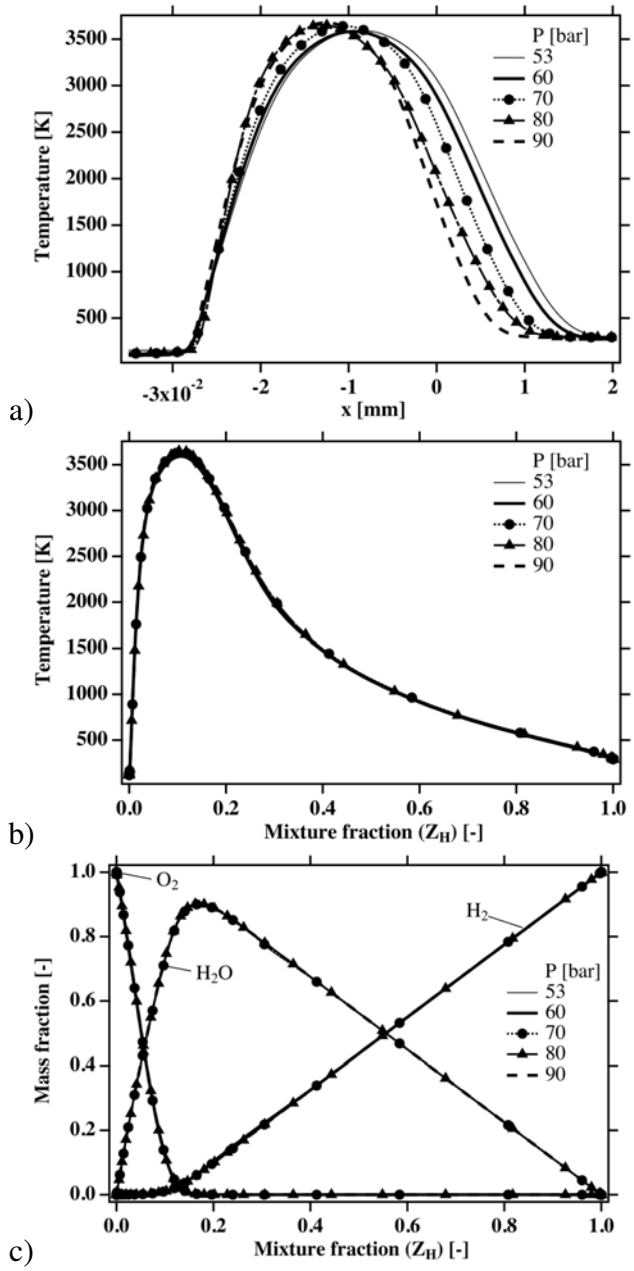

Figure 4.5. Pressure effect on the counter flow flame. a) Temperature distribution in physical space, b) and c) temperature distribution and mass fractions of principal species in mixture fraction space. ($a = 10^5 s^{-1}$).

Combustion model definition

The ultimate goal of this study is to develop a combustion model that reproduces the flame behavior in the VC burner, where pressure waves and turbulent strain variations are present. This implies that the energy (or enthalpy) transport equation must be conserved in the system and that the flame must be represented as a source term. For this situation, the system of equations reduces to:

- Mass:

$$\frac{\partial \rho}{\partial t} + \nabla \cdot (\rho \mathbf{u}) = 0. \tag{4.5}$$

- Momentum:

$$\frac{\partial}{\partial t}(\rho \mathbf{u}) + \nabla \cdot \left[\rho \mathbf{u} \otimes \mathbf{u} + \frac{p}{M^2}\mathbf{I}\right] = \nabla \cdot \tau, \tag{4.6}$$

- Mixture fraction:

$$\frac{\partial}{\partial t}(\rho Z) + \nabla \cdot (\rho Z \mathbf{u}) = \nabla \cdot \mathbf{q}_Z, \tag{4.7}$$

  where

$$\mathbf{q}_Z \;=\; \rho D_Z \nabla Z, \tag{4.8}$$

  here D_Z is chosen to have $Le_Z = 1$ (Le_Z is the Lewis number of Z),

- Total non-chemical energy:

$$\frac{\partial}{\partial t}(\rho E) + \nabla \cdot [(\rho E + P)\mathbf{u}] = \nabla \cdot \left[-\mathbf{q}_E^{model} + M^2(\tau \cdot \mathbf{u})\right] + \dot{Q}_E^{model}, \tag{4.9}$$

  where the energy diffusion flux is modeled by the relation :

$$\mathbf{q}_E^{model} = -\lambda \, \nabla T \, + \, \mathbf{q}_Z \, (h_s^{H_2} - h_s^{O_2}) \, , \tag{4.10}$$

  where $h_s^{H_2}$ and $h_s^{O_2}$ are the sensitive enthalpies of hydrogen and oxygen, respectively.

  $\dot{Q}_E^{model}$ is the model source term representing the flame.

  A direct tabulation of the energy source term is not an optimal approach for two reasons. First, heat release is a very non-linear term that would significantly increase interpolation errors. Second, heat release is sensitive to strain rate and pressure variations (contrary to the flame temperature), then a tabulation of this source term would require additional dimensions, degrading interpolation accuracy.

  Another method is to rely on the fact that the flame temperature is almost insensitive to thermodynamic and flow conditions. It is then possible to define a source term that allow us to recover the correct temperature:

$$\dot{Q}_E^{model} \approx \Gamma \frac{(\rho \, h_t)^{flame} - \rho \, h_t}{\Delta t}, \tag{4.11}$$

where h_t^{flame} and ρ^{flame} are the total sensitive enthalpy and the density in the flame respectively, Δt is the time step in the computation and Γ is test function that detects the flame zone.

In preliminary studies it was shown the reaction zone is not significantly affected by pressure and temperature variations contrary to non-reacting regions. To make the solver capable of reproducing compressibility and temperature effects, the model source term must modify the enthalpy in the flame zone only.

Consequently, a flame detection function Γ is employed, which is equal to unity in the flame front and zero otherwise. This function is defined as:

$$\Gamma = \frac{1}{2}\left(1 + tanh\left(\frac{Z - Z_{min}^{flame}}{\Delta_Z}\right)\right) \times \frac{1}{2}\left(1 - tanh\left(\frac{Z - Z_{max}^{flame}}{\Delta_Z}\right)\right), \tag{4.12}$$

where Z_{min}^{flame} and Z_{max}^{flame} are the flame boundaries in mixture fraction space, and Δ_Z controls the smoothness of the test function. From previous results, the flame is located in the range: $0.01 < Z < 0.99$ and an optimal value of $\Delta_Z = 5 \times 10^{-3}$ is used.

Combustion model performance

The model was compared to detailed calculations to assess its performance and sensitivity to strain and pressure. Figure 4.6 presents a comparison between DNS results and profiles given by the combustion model. General good agreement is observed between the two. The flame structure obtained with the model is slightly thinner than the reference flame, but the maximum temperature is recovered correctly. Figure 4.6a shows the corresponding species profiles extracted from the table. Good agreement is observed between the model and the reference calculation, with only minor differences on the hydrogen side.

Figures 4.6b) and c) present the sensitivity of the model to strain rate and pressure. The previous investigation showed that the strain rate modifies the thickness of the reaction zone due to dynamic effects. Figure 4.6b) confirms that the model reproduces the same trend, giving the correct thickness of the flame region.

The fact that the flame sensitivity to strain rate variations is correctly captured, indicates that the model is able to predict the heat release rate dependency on strain. Indeed, it was shown earlier that for hydrogen - oxygen combustion, the fast chemistry assumption applies. In this case, heat release compensates exactly for heat losses due to diffusion processes [18]:

$$\dot{\omega}_T = -\frac{1}{2}\,\rho\chi\,\frac{\partial^2 T}{\partial Z^2} \tag{4.13}$$

In this equation, the term $\rho\chi$ comes from mixing processes and is obtained using the governing equations. The other term : $\partial^2 T/\partial Z^2$ represents the chemical effects and is extracted from the

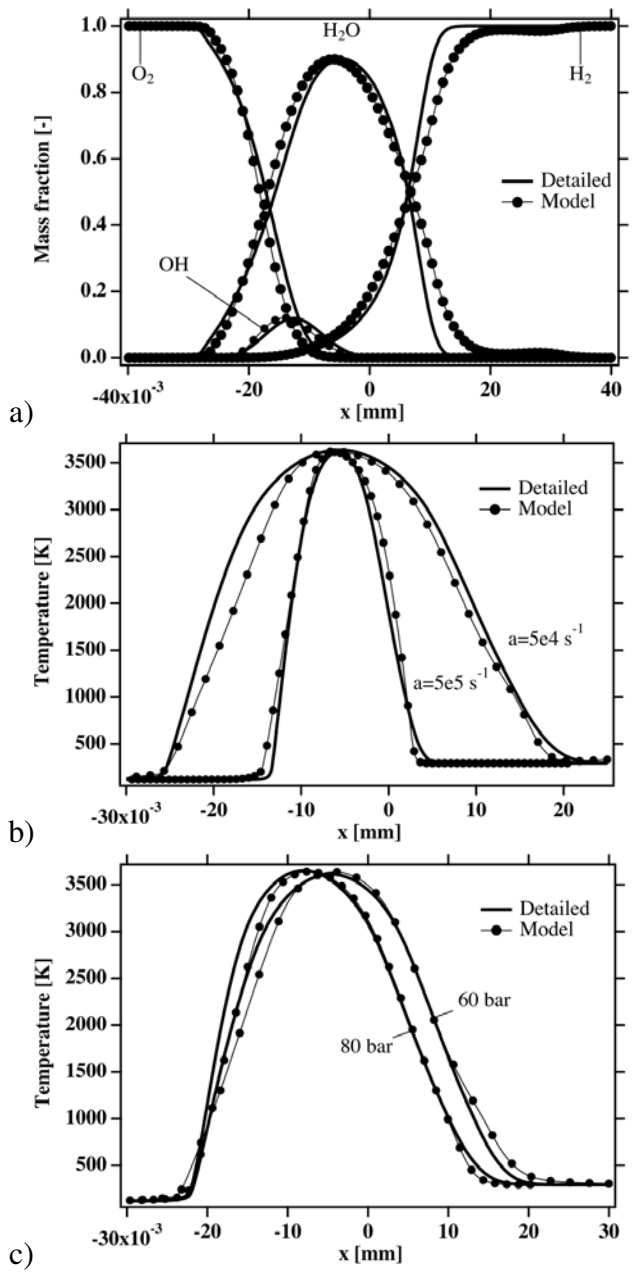

Figure 4.6. Comparison between the model and the detailed computations : a) mass fraction profiles of major species, b) Sensitivity of the model to strain rate and c) sensitivity of the model to pressure.

tabulation of the model. This term was shown to be invariant with respect to strain and pressure. Consequently, the model naturally recovers the impact of strain and pressure (through the term $\rho\chi$) even though a one dimensional manifold ($Z \rightarrow (Y_i^{table},\ T^{table})$) is employed. The ability of the

model to capture this effect is crucial since the coupling between local strain rate and heat release plays an important role in combustion stability processes.

The sensitivity of the model to pressure variations is also correctly recovered as shown in Fig. 4.6c. The impact of pressure on the flame thickness is captured with a satisfactory accuracy. This aspect is also a requirement for the study of flame stability in high pressure combustors. Pressure and strain rate fluctuations both result in local variations of heat release that can excite the acoustic modes of the burner and lead to combustion instabilities.

This model has been use in the three-dimensional configuration and performance of the model is presented in Fig. 4.7:

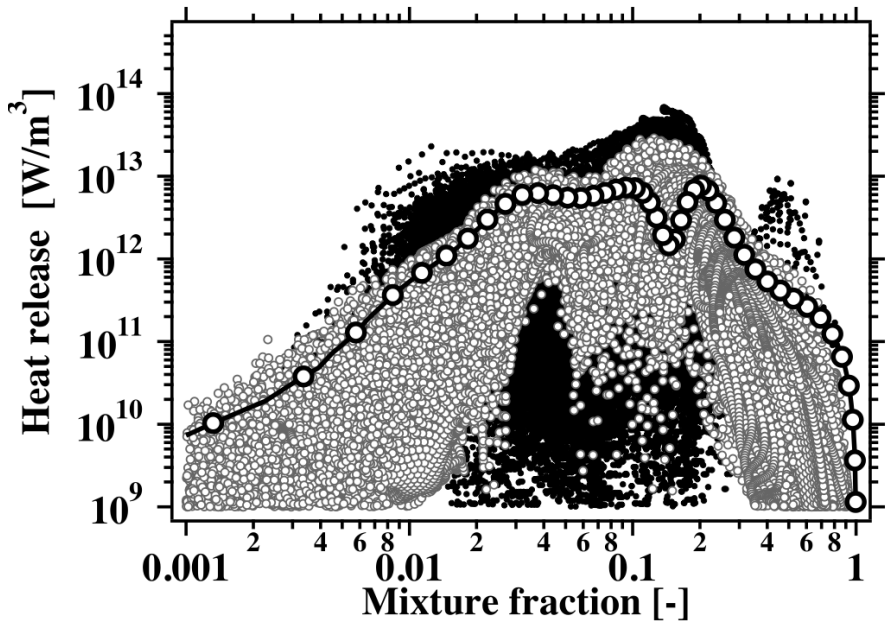

Figure 4.7. Scatter plot of the heat-release with respect to mixture fraction in the DNS computations. (○) detailed chemistry, (●) flamelet model and (− ○ −) counter-flow calculation $a = 1 \times 10^5 s^{-1}$.

Figure 4.7 shows a scatter plot of heat-release in mixture fraction space for the detailed chemistry and the flamelet approaches. For comparison, the heat-release profile of a laminar counter-flow flame at a strain rate of $a = 5 \times 10^5 s^{-1}$ has been added to the figure. This comparison shows that the flamelet model is able to predict heat-release variations due to local turbulence fluctuations. It is recalled that the in present flamelet approach, the scalar dissipation rate is not an input of the look-up table, nonetheless, the model is able to predict strain effects. The reason is that under the infinitely fast reaction assumption, heat release is limited by diffusion processes [18]. In other words, when strain is increases, more fuel and oxidizer is provided to the flame and heat

release is enhanced (pressure has a similar impact). In Figure 4.7 one can observe that for a given value of the mixture fraction, the heat-release envelop is broader for the flamelet model than for the detailed chemistry approach. Two main reasons can explain these differences. First, the thermal diffusion flux is slightly larger in the model due to the unity Lewis number assumption. Second, these scatter plots are obtained from instantaneous solutions and local strain rates may be different. The heat-release distributions obtained in the DNS for both the detailed chemistry and the flamelet approaches are in agreement with the profile extracted from a laminar counter-flow calculation. This observation shows that in the present configuration, the flame can be viewed as an ensemble of non-premixed laminar opposed-jet flames experiencing different strain rates locally. Using the model, the computational time has been improved by a factor of five compared to the detailed chemistry method. The main reason is that the present approach carries only one equation for mixture fraction whereas in the detailed framework, height species are transported. The net computational benefit is not a factor height because thermodynamic and transport schemes still rely on the height species (read in the look-up table).

This page intentionally left blank.

Chapter 5

Conclusions

The main objective of the present work was to study stabilization processes of a lifted hydrogen flame in a vitiated environment at elevated pressure. The second aspect of the work was to develop a combustion model capable of taking into account pressure and strain effects in high-Reynolds number flows, as flame stability in high pressure devices is affected by pressure and local strain fluctuations. The present work covered most of these two points.

First, a systematic approach has been employed to define the optimal LES configuration that will provide the best accuracy of LES results will minimizing computational time. In this step, a resolution criterion has been established based on the first moment of turbulence. The optimal grid spacing is obtained when the mean and rms of the velocity become insensitive to the level of refinement. In the present case, 40 points in the diameter provide convergence of the turbulence statistics.

Second, a literature review of previous investigations suggests that a *flamelet* approach based on tabulated chemistry is appropriate. Thus, to define the relevant model parameters, the first step was to study the flame structure and its sensitivity to strain and pressure under realistic flow conditions. A canonical opposed-jet configuration was designed to perform the study. Analysis revealed that the flame is thin and very robust over a large range of strain rates. This validates the *flamelet* assumption, and allows one to simplify the modeling approach since scalar dissipation rate can be ignored in the model tabulation. In addition, it was shown that pressure has a limited impact on flame structure in mixture fraction space at supercritical pressures. Thus, it can be omitted as a table input parameter. However, pressure and strain rate fluctuations induce variations in heat release. To take these effects into account, the governing system must include a transport equation for energy. Strain effects are naturally reproduced by solving mass, momentum, and mixture fractions transport equations. Based on these conclusions, a flamelet-like approach has been defined that takes into account compressibility and strain effects.

The flamelet approach is coupled with a compressible governing system to handle high-pressure effects. In the flame region, the enthalpy is modified by a compressible source term (Eq. 4.11) to recover the correct temperature field. This source term is evaluated from the local pressure and enthalpy (from the governing system and the equation of state) and from the table outputs T^{table} and Y_i^{table} (that are insensitive to strain and pressure effects in the present case). To clearly explain why this model is able to capture pressure and strain rate effects, although it is based on an one-dimensional tabulation ($Z \rightarrow \ T^{table}$, Y_i^{table}), one can recast the model source term as: $\dot{\omega}_T = -1/2 \ \rho\chi \ \partial^2 T/\partial Z^2$. The term $\partial^2 T/\partial Z^2$, which represents chemical effects and for

the present conditions is insensitive to strain and pressure, can be model with a one-dimensional flamelet manifold. The second term $\rho\chi$ represents mixing effects, which are evaluated through the governing system. It is this latter term that embeds pressure and strain rate effects.

The model was implemented in the LES solver and its accuracy was tested in a laminar opposed-jet configuration. Model sensitivity to strain rate and pressure was tested and good agreements were obtained in comparison with detailed computations. In particular, the impacts of strain and pressure on local heat release rate were correctly recovered. This capability of the model is a requirement to study combustion stability high-pressure high-Reynolds number devices.

In future work we will focus on the partially premixed combustion mode of the flame that must be incorporated in the model to predict stabilization. Preliminary results show that a new dimension (progress variable) must be added to the look-up table to capture unsteady partially premixed effects.

References

[1] Buelow, P., Venkateswaran, S., Merkle, C.: Effect of grid aspect ratio on convergence. AIAA Journal**32**(12), 2401–2408 (1994)

[2] Chehroudi, B.: Physical Hypothesis for the Combustion Instability in Cryogenic Liquid Rocket Engines. Journal of Propulsion and Power**26**(6), 1153–1160 (2010)

[3] Choi, Y., Merkle, C.: Time-derivative preconditioning for viscous flows. In: AIAA 22nd Fluid Dynamics, Plasma Dynamics and Lasers Conference. Sverdrup Technology, Incorporated, Lewis Research Center Group (1991)

[4] Choi, Y., Merkle, C.L.: The application of preconditioning in viscous flows. Journal of Computational Physics **105**(2), 207–223 (1993)

[5] Ely, J., Hanley, H.J.M.: Prediction of transport properties. 2. Thermal conductivity of pure fluids and mixtures. Industrial & Engineering Chemistry Fundamentals **22**(1), 90–97 (1983)

[6] Gaitonde, A.L.: A dual-time method for two-dimensional unsteady incompressible flow calculations. International journal for numerical methods in engineering **41**(6), 1153–1166 (1998)

[7] Harlow, F., Welch, J.: Numerical calculation of time-dependent viscous incompressible flow of fluid with free surface. Physics of Fluids**8**(12), 2182–2189 (1965)

[8] Harrje, D., Reardon, F.: Liquid propellant rocket instability. Tech. Rep. Report SP-194, NASA (1972)

[9] Hirschfelder, J., Curtiss, F., Bird, R.: Molecular theory of gases and liquids. John Wiley & Sons, New York (1964)

[10] Jameson, A., Schmidt, W., Turkel, E.: Numerical solution of the euler equations by finite volume methods using runge-kutta time stepping schemes. In: A.p. 81-1259 (ed.) 14th Fluid and Plasma Dynamic Conference. Palo Alto (1981). Ref lolo

[11] Jorgenson, P., Turkel, E.: Central difference tvd schemes for time dependent and steady state problems. Journal of Computational Physics **107**(2), 297 – 308 (1993). DOI 10.1006/jcph.1993.1145. URL http://www.sciencedirect.com/science/article/pii/S0021999183711459

[12] Klein, M., Sadiki, A., Janicka, J.: A digital filter based generation of inflow data for spatially developing direct numerical or large eddy simulations. Journal of Computational Physics **186**(2), 652–665 (2003)

[13] Knapp, B., Farago, Z., Oschwald, M.: Interaction of LOX/GH2-Spray Combustion with Acoustics. In: 45th AIAA, Reno, NV, pp. 1–9 (2007)

[14] Merkle, C., M., A.: Time-accurate unsteady incompressible flow algorithms based on artificial compressibility. In: 8th Computational Fluid Dynamics Conference, vol. 32, pp. 2401–2408 (1987)

[15] Oefelein, J.C.: Simulation and analysis of turbulent multiphase combustion processes at high pressures. MI Dissertations Publishing (1997). URL http://search.proquest.com/docview/304367555?accountid=27673

[16] Oefelein, J.C.: Thermophysical characteristics of shear-coaxial lox–h2 flames at supercritical pressure. Proceedings of the Combustion Institute**30**(2), 2929–2937 (2005)

[17] Oefelein, J.C.: Mixing and combustion of cryogenic oxygen-hydrogen shear-coaxial jet flames at supercritical pressure. Combustion Science and Technology**178**(1-3), 229–252 (2006)

[18] Poinsot, T., Veynante, D.: Theoretical and numerical combustion. R.T. Edwards, 2nd edition. (2005)

[19] Reid, R.C., Prausnitz, J.M., Polling, B.E.: The properties of liquids and gases, vol. fourth ed. McGraw Hill, New York (1987)

[20] Ribert, G., Zong, N., Yang, V., Pons, L., Darabiha, N., Candel, S.: Counterflow diffusion flames of general fluids: Oxygen/hydrogen mixtures. Combustion and Flame **154**, 319–330 (2008)

[21] Roe, P.: Approximate riemann solvers, parameter vectors and difference schemes. Journal of Computational Physics**43**, 357–372 (1981)

[22] Roe, P.: Characteristic-based schemes for the euler equations. Annual review of fluid mechanics **18**(1), 337–365 (1986)

[23] Searby, G., Nicole, A., Habiballah, M., Laroche, E.: Prediction of the efficiency of acoustic damping cavities. Journal of Propulsion and Power**24**(3), 516–523 (2008)

[24] Swanson, R.C., Turkel, E.: On central-difference and upwind schemes. Journal of Computational Physics**101**(2), 292 – 306 (1992). DOI 10.1016/0021-9991(92)90007-L. URL http://www.sciencedirect.com/science/article/pii/002199919290007L

[25] Takahashi, S.: Preparation of a generalized chart for the diffusion coefficients of gases at high pressures. journal of Chemical Engineering of Japan **7**(6), 417–420 (1974)

[26] Van Albada, G., Van Leer, B., Roberts Jr, W.: A comparative study of computational methods in cosmic gas dynamics. Springer (1997)

[27] Van Leer, B.: Towards the ultimate conservative difference scheme. ii. monotonicity and conservation combined in a second-order scheme. Journal of Computational Physics **14**(4), 361 – 370 (1974). DOI 10.1016/0021-9991(74)90019-9. URL http://www.sciencedirect.com/science/article/pii/0021999174900199

[28] Van Leer, B.: Towards the ultimate conservative difference scheme IV. A new approach to numerical convection. Journal of Computational Physics**23**, 276–299 (1977)

[29] Venkateswaran S.and Merkle, C.L.: Dual time-stepping and preconditioning for unsteady computations. AIAA journal (95-0078) (1995)

[30] Weiss, J.M., Smith, W.A.: Preconditioning applied to variable and constant density flows. AIAA journal **33**(11), 2050–2057 (1995)

[31] Withington, J., Yang, V., Shuen, J.: A time-accurate implicit method for chemically reacting flows at all mach numbers. In: 29th AIAA Aerospace Sciences Meeting, vol. 1 (1991)

[32] Yang, V., Anderson, W.: Liquid rocket engine combustion instability. Aiaa (1995)

DISTRIBUTION:

1	MS 0359	D. Chavez, LDRD Office, 898
1	MS 0899	Technical Library, 8944 (electronic copy)

Sandia National Laboratories